Influence of chemical conversion parameters and resulting PbI2 content on carrier density and morphology of the p-type electrodeposited hybrid perovskite CH3NH3PbI3

Youssof Dandal, Cyrille Bazin, Francoise Pillier, Hubert Cachet, Alain Pailleret

Journal Pre-proof

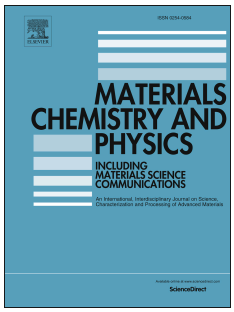

Influence of chemical conversion parameters and resulting PbI_2 content on carrier density and morphology of the p-type electrodeposited hybrid perovskite $CH_3NH_3PbI_3$

Youssof Dandal, Cyrille Bazin, Francoise Pillier, Hubert Cachet, Alain Pailleret

PII: S0254-0584(23)00641-7

DOI: https://doi.org/10.1016/j.matchemphys.2023.127933

Reference: MAC 127933

To appear in: *Materials Chemistry and Physics*

Received Date: 10 January 2023

Revised Date: 12 April 2023

Accepted Date: 15 May 2023

Please cite this article as: Y. Dandal, C. Bazin, F. Pillier, H. Cachet, A. Pailleret, Influence of chemical conversion parameters and resulting PbI_2 content on carrier density and morphology of the p-type electrodeposited hybrid perovskite $CH_3NH_3PbI_3$, *Materials Chemistry and Physics* (2023), doi: https://doi.org/10.1016/j.matchemphys.2023.127933.

Credit Author Statement

Youssof DANDAL : *Conceptualization, Methodology, Formal analysis, Investigation, Writing-Original Draft, Vizualisation*

Cyrille BAZIN : *Investigation, Resources, Vizualisation*

Françoise PILLIER : *Investigation, Resources, Vizualisation*

Hubert CACHET : *Validation, Writing – Review & Editing*

Alain PAILLERET : *Conceptualization, Methodology, Formal analysis, Writing – Review & Editing, Vizualisation, Supervision, Project administration, Funding acquisition*

Influence of chemical conversion parameters and resulting PbI_2 content on carrier density and morphology of the p-type electrodeposited hybrid perovskite $CH_3NH_3PbI_3$

Youssof Dandal[a], Cyrille Bazin[a], Françoise Pillier[a], Hubert Cachet[a], Alain Pailleret[a]

[a] *Sorbonne Université, CNRS, Laboratoire Interfaces et Systèmes Electrochimiques (LISE, UMR 8235), 4 place Jussieu, F-75005, Paris, France*

Abstract

Carrier density of electrodeposited methylammonium lead iodide perovskite ($CH_3NH_3PbI_3$) can be modulated inside the 10^{17} to 10^{20} cm^{-3} range by carefully selecting the experimental parameters used during the last two chemical conversion steps of their synthesis. This finding has been made possible by performing systematically Mott-Schottky (MS) plots in aqueous solution on various semi-conducting $CH_3NH_3PbI_3$ perovskite samples. These latter were produced by a three-step synthesis method combining an electrodeposition step with two consecutive chemical conversion steps. In a first step, the galvanostatic electrodeposition of a lead dioxide (PbO_2) thin film is carried out. This latter is then converted into lead (II) iodide (PbI_2) by immersion in a HI/ethanol solution, this latter being then itself turned in a third and last step into the well-known $CH_3NH_3PbI_3$ perovskite by a new immersion step in a methylammonium iodide (MAI)/isopropanol solution. This very simple and highly reproducible synthesis method allows the production of perovskite thin films on large surfaces, unlike many other synthesis methods of perovskite thin films. In parallel to the determination of p-type character, carrier concentration and flat band potential of the perovskite samples using Mott-Schottky plots, their chemical composition, their morphology and their crystallinity were

characterized by using scanning electron microscopy (SEM) and X-Ray Diffraction (XRD) and compared with those of the products obtained at the end of each of the two first steps, i.e. PbO_2 and PbI_2 respectively. Interestingly, it was shown that the final product is not always a pure p-type perovskite thin film as various amounts of lead (II) iodide (PbI_2) can be detected depending on the experimental parameters used during the two consecutive chemical conversion steps. The main result of this study is that the dopant concentration of perovskite thin films was shown to be inversely proportional to the amount of the remaining PbI_2 impurities detected in the bulk of perovskite thin films.

Keywords : Electrodeposition, hybrid perovskites, semiconductors, Mott-Schottky plots, lead iodide.

Introduction

Perovskites have recently become exciting low-cost candidates for (high energy) photodetectors [1,2] and photovoltaic (PV) devices applications [3]. Similarly to organic solar cells (OSCs) [4], the power conversion efficiency (PCE) of perovskite solar cells (PSCs) has increased a lot over the last decade, from 3.8 % in 2009 [5] to 25 % in 2019 [6]. This impressive increase triggered the huge development of perovskites [7], a large family of fascinating materials, among which one can find organic lead halide perovskites (OLHP) [8]. In this well-known family of ionic solids, one can find the methylammonium lead iodide perovskite ($CH_3NH_3PbI_3$, often abbreviated as $MAPbI_3$ in literature), with unique properties such as an adjustable band gap close to 1.55 eV [9], an absorption coefficient of 10^5 cm^{-1} in the visible range superior to that of c-Si [10], a long carrier diffusion length, and an excellent mobility of both types of photogenerated carriers, i.e. electrons and holes. Nowadays, it is a standard perovskite absorber in PV cells that is often considered as a rare intrinsic semi-conductor possessing an ambipolar carrier mobility. Even if valence and conduction bands were found to

consist mainly of iodine and lead orbitals, extensive first-principles and force-field calculations studies revealed that MAI was shown to have a strong influence on the structural and optical properties (band gap) of OLHP through dynamic hydrogen bonding [11]. OLHPs are still widely investigated nowadays so as to i) better understand and optimize their opto-electronic properties, and ii) reduce their toxicity that results from the combination of the presence of lead in their chemical composition with their lack of stability. Many strategies involving interface modification and aimed at improving their efficiency and their stability have been suggested recently in literature [12–14] and they appear to be more promising than that relying on the development of lead-free (or lead-less) perovskites [15] at the present stage of research in this field. In parallel, further efforts aimed at understanding the doping mechanism of perovskites are necessary in order to optimize their electronic properties for rational design of efficient PV devices [16]. In fact, Kim *et al.* [17] had found out that bulk perovskites could actually be self-doped (p type or n-type) by controlling their growth conditions. Moreover, Wang *et al.* [16] have also reported that hybrid $CH_3NH_3PbI_3$ perovskite films could actually act as p-type or n-type semiconductors depending on the CH_3NH_3I:PbI_2 ratio. Those rich in methylammonium iodide (MAI) behave as p-type semiconductors, whereas those richer in PbI_2 are n-type semiconductors.

Various synthesis methods allowing the production of hybrid perovskites have been reported in literature [18]. They can be divided into two families that are the vapour phase deposition and the scalable deposition methods. Vapour phase deposition methods such as physical vapor deposition (PVD) [19], and chemical vapor deposition (CVD) [20] require highly expensive vacuum and temperature operations as well as long deposition times that could potentially hinder their application for low cost fabrication of photovoltaic devices. Among scalable deposition methods, spin coating is the most common, useful and inexpensive method for the fabrication of perovskite solar cell devices [5,21,22]. However, this method is only suitable for

small area deposition on flat substrates and it produces undesirable highly rough and porous surfaces [23], which limits its commercial use. Several other scalable deposition methods were also employed such as atomic layer deposition (ALD) [24], spray deposition (SD) [25], and doctor blade technique (DB) [26].

Therefore, one of the current challenges is an urgent need to develop new alternative methods to produce perovskite solar cells (PSC) in a large-scale, high-quality layer and low-cost manufacturing process to produce high-efficiency PSCs.

On the other hand, electrodeposition, another member of the family of scalable solution deposition methods, combines the advantages of both vapor phase deposition and spin coating as it is applicable for larger areas, fast, inexpensive, and it does not require the use of toxic solvents. Besides, electrodeposition, and electrochemically assisted deposition techniques, were shown over recent decades to be fully relevant for the production of insulating, semi-conducting or conducting thin layer materials such as polymers [27,28], metals [29], inorganic materials [30], composite materials (such as conducting polymers incorporating nanomaterials for example) [31–34] and transition metal oxides [35,36], some of which are obtained as a crystalline and/or nanostructured variety either immediately or after an annealing procedure.

In spite of its obvious advantages and promises, electrodeposition remains largely underestimated in literature nowadays [13,18]. Very few studies have developed very simple conversion steps in solution to change electrodeposited PbO_2 thin films into perovskites through ion exchange and/or addition and they report only very rarely the identification of the semi-conductor type (n- or p-) of the resulting perovskites [37–39]. In this respect, the combination of electrodeposition with very simple chemical conversion steps in solution could be a very interesting technique as it could easily become an inexpensive and mature industrial technique for the manufacturing, with a rapid deposition rate, of perovskite thin films of large-scale of the order of square meters and with complex shapes [40].

In order to strengthen the attractiveness of the electrodeposition method for the synthesis of p-type perovskite thin films, its ability to allow an accurate tuning of their carrier concentration is highlighted herein through a better understanding of the chemical conversion mechanisms occurring during the two consecutive immersion steps in alcoholic solutions. In particular, an obvious relation between the remaining PbI_2 fraction identified and evaluated with the help of XRD and EDS analysis and the carrier concentration determined by Mott-Schottky measurements in the final perovskite thin films is convincingly demonstrated.

Experimental part

1. Synthesis of $CH_3NH_3PbI_3$ perovskite thin films

Figure 1 schematically illustrates the three different steps involved in the production of $CH_3NH_3PbI_3$ perovskite thin films on a glass/fluorine-doped tin oxide (FTO) substrate.

Step 1: Electrodeposition of PbO_2

Glass/fluorine-doped tin oxide (FTO) substrates (1.5 x 1.5 cm) purchased from SOLEMS (Palaiseau, France) were sonicated in ethanol for 15 minutes, then washed with deionized water. They were then used as working electrodes for the electrodeposition of lead dioxide (PbO_2) thin films using either one or the other of the two following electrolytic aqueous solutions:

S_a: $Pb(NO_3)_2$ (0.1 M), $NaNO_3$ (0.2 M), HNO_3 (0.1 M) in water

S_b: $Pb(CH_3COO)_2$ (0.1 M), CH_3COONa (1.0 M) in water

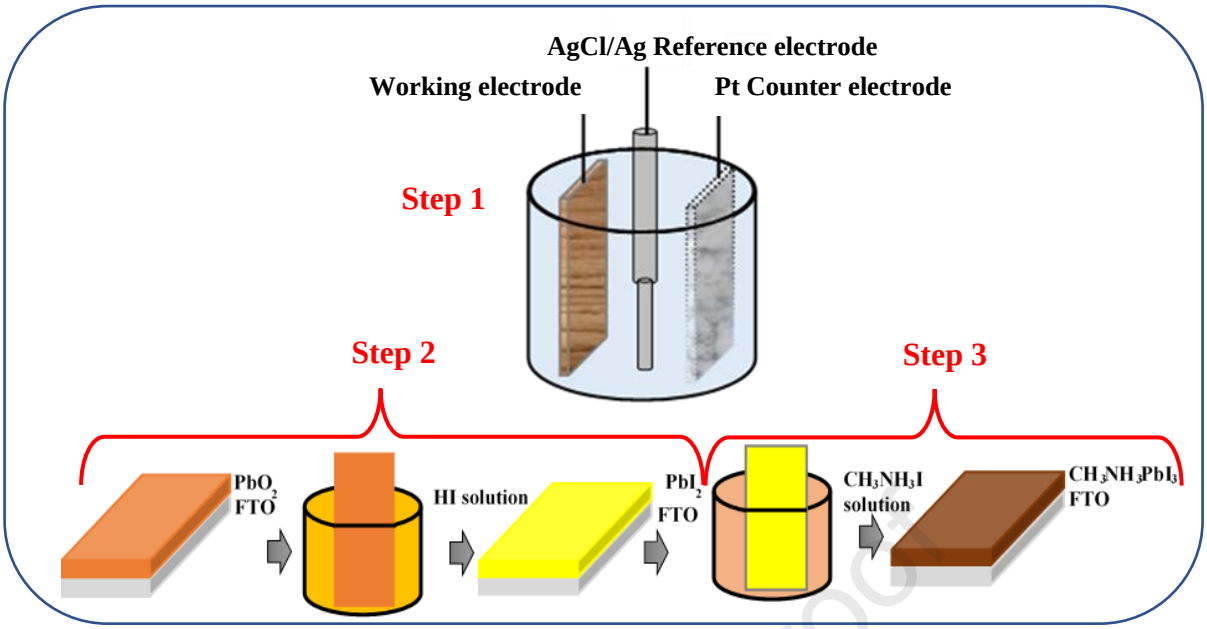

Figure 1 : Schematic illustration of the $CH_3NH_3PbI_3$ perovskite film formation on a glass/FTO substrate starting from the electrodeposition of PbO_2 layer from either S_a or S_b (step 1) and its subsequent conversions first in PbI_2 by immersion in a HI/ethanol solution (step 2) and finally in $CH_3NH_3PbI_3$ by immersion in a MAI/isopropanol solution (step 3).

The electrodeposition was conducted in a standard three-electrode electrochemical cell using a FTO/glass substrate, a Pt grid and a KCl saturated AgCl/Ag electrode as working, counter and reference electrodes, respectively. They were immersed in S_a or S_b (step 1) and connected to a Biologic VSP potentiostat so as to carry out the electrodeposition in galvanostatic conditions at room temperature using the chronopotentiometry technique. The electrodeposition current and duration were set at 0.560 mA and 3 minutes, respectively. After electrodeposition, one can easily observe on the working electrode (i.e. the glass/FTO substrate) a light brown film whose color confirms the formation of PbO_2. Finally, the obtained films were washed thoroughly with deionized water and dried in air at room temperature.

Step 2: Conversion of PbO_2 into PbI_2

The conversion of PbO_2 into PbI_2 was achieved by immersing the obtained PbO_2 films in a HI (0.05 M)/ethanol solution ($\mathbf{S_c}$) at room temperature during 5 minutes for the PbO_2 layers obtained from nitrate solution ($\mathbf{S_a}$), and for 1 to 15 minutes for the PbO_2 layers obtained from acetate solution ($\mathbf{S_b}$). The color of the layers then turned from light brown to bright yellow. The

obtained PbI_2 layers were then washed thoroughly with ethanol and dried in air at room temperature. The PbI_2 layers obtained after a 5 minutes immersion in $\mathbf{S_a}$ were denoted as D_1, whereas those obtained by immersion in S_b were denoted as D_2.

Step 3: Conversion of PbI_2 into $CH_3NH_3PbI_3$

In a preliminary step, the methylammonium iodide (CH_3NH_3I) salt was synthesized according to the procedure described in the supplementary Information (see section I) and then used to prepare $\mathbf{S_d}$ solutions.

PbI_2 thin films obtained after immersion of PbO_2 layers in $\mathbf{S_b}$ at different immersion times were converted into $CH_3NH_3PbI_3$ thin films by immersion in a $\mathbf{S_d}$ solution (CH_3NH_3I/isopropanol solution, 25 mg/mL) for durations varying between 20 and 180 minutes. During this step, the color of the film turned from bright yellow to dark brown (see Figure 1, step 3).

2. Structural characterization of the layers

The morphology, thickness and elemental chemical composition (atomic percentage) of the obtained layers were evaluated using scanning electron microscopy combined with EDS (SEM, Ultra55, Zeiss). Diffractograms were recorded on an Empyrean Panalytical X-Ray Diffractometer with Cu Kα radiation (K = 0.15418 nm) to evaluate the crystallinity of the various layers synthesized in this work.

3. Opto-electronic characterization of the layers

A U4001 spectrophotometer (Hitachi) was used to acquire absorbance spectra of PbI_2 and $CH_3NH_3PbI_3$ films. All spectra were baseline corrected so as to eliminate the contribution of light absorption by the fluorine-doped tin oxide coated glass slides. The absorption coefficient was determined as a function of the wawelength for each of the samples by using the following equation:

$$\alpha(\lambda) = 2.303\ \mathrm{Abs}(\lambda)/\mathrm{d} \quad (1)$$

In this equation, α(λ) and Abs(λ) are respectively the absorption coefficient and the absorbance for a given wavelength, and d is the thickness of the thin film sample (this latter was measured using SEM-FEG for our PbI_2 or perovskite samples). Equation (1) is a very simplified version of the expression of the transmittance as a function of the refractive indices of the substrate (i.e. glass/ITO) and the sample (PbI_2 or perovskite). It was shown to be valid only for the high absorption region of the absorbance spectrum, for a zero reflectance, and on condition that both refractive indices be between 1.5 and 2 [41]. As a consequence, equation (1) will provide only a raw estimation of the α(λ) values. These latter were used nevertheless to build Tauc plots from which the optical band gap was determined for each sample.

Mott-Schottky measurements were performed with the help of a three electrode electrochemical cell including the glass/FTO/perovskite (or glass/FTO/PbI_2) sample as a working electrode and a platinum grid as a counter electrode. The reference electrode, a silver wire immersed in a 0.01 M $AgNO_3$/acetonitrile solution ($E(Ag^+(10\ mM)/Ag) = 0.68$ V vs. SHE), was protected using a bridge tube filled with a 0.1 M tetrabutylammonium hexafluorophosphate ($TBAPF_6$)/CH_2Cl_2 solution (**S_e**). During experiments, this latter was immersed in an electrochemical cell containing also **S_e** and the cell was kept closed to prevent solvent evaporation and to keep the working electrode area constant. Measurements were performed over a 0 to 1 V potential range and over a 500 Hz - 10 kHz frequency range using a 10 mV sine amplitude.

Results and discussion

1. Synthesis of PbO_2, PbI_2 and $CH_3NH_3PbI_3$ layers

In our investigations as well as in literature, it was shown that PbO_2 thin films can be successfully electrodeposited from either nitrate (S_a) or acetate (S_b) aqueous electrolytic

solutions with a similar electrodeposition mechanism in both cases. In a preliminary study aimed at confirming this latter, a linear sweep voltammogram (LSV) was obtained between 0 and 1.5 V vs. ref. using a 100 $mV.s^{-1}$ scan rate in an electrolytic acetate aqueous solution (S_b without lead (II) acetate, pH ≈ 8, see blue curve in inset of Figure 2). It shows a weak oxidation peak between 1.1 and 1.3 V vs. AgCl/Ag that is attributed to surface oxidation of bare FTO working electrode. It is followed by a fast increase of current with the anodic potential that reveals water oxidation into dioxygen. In a similar electrolytic solution containing moreover lead (II) acetate at a 0.1 M bulk concentration (pH ≈ 8), i.e. in S_b, a LSV obtained in the same potential range with the same scan rate shows a very intense oxidation current between 1.03 and 1.5 V vs. AgCl/Ag (see red curve in inset of Figure 2) that results from the oxidation of Pb^{2+} into Pb^{4+}, allowing thus the anodic electrodeposition of PbO_2.

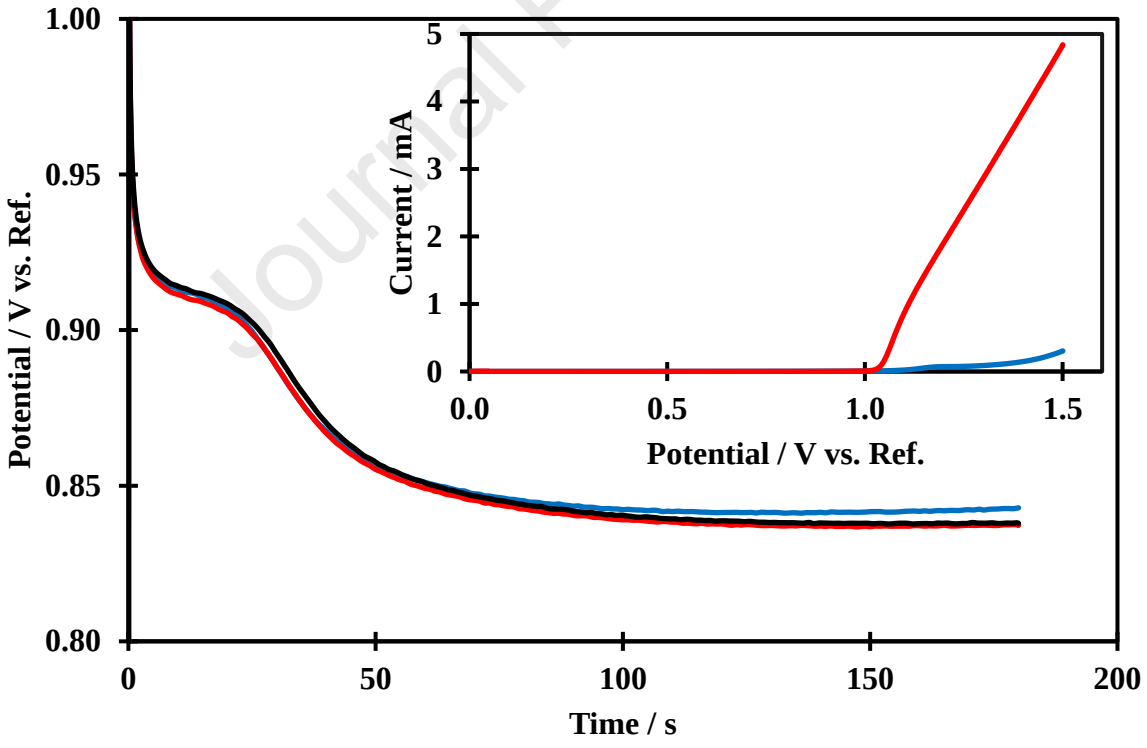

Figure 2 : Galvanostatic electrodeposition (chronopotentiometry) curves allowing the production of PbO_2 thin films on glass/FTO working electrodes. Imposed current: 0.56 mA. Electrodeposition time: 3 min. Inset: LSV curves performed in acetate aqueous electrolytic solutions in the absence (S_b without $Pb(CH_3COO)_2$, see blue curve) or in the presence of lead (II) acetate (S_b, see red curve). Scan rate: 100 $mV.s^{-1}$. Potentials are expressed in V vs. AgCl/Ag.

Table 1 : Different synthesis parameters of PbO_2, PbI_2 and $CH_3NH_3PbI_3$ thin films.

Films	$NaNO_3$ Solution (S_a) for electrodeposition	CH_3COONa Solution (S_b) for electrodeposition	Electrodeposition duration of PbO_2 / min	Immersion duration of PbO_2 in S_c (conversion to PbI_2) / min	Immersion duration of PbI_2 in S_d (conversion to $CH_3NH_3PbI_3$) / min
D_1	✓	—	**2**	**5**	—
D_2	—	✓	**2**	**5**	—
S_1	—	✓	**3**	**1**	**180**
S_2	—	✓	**3**	**2**	**180**
S_3	—	✓	**3**	**3**	**180**
S_4	—	✓	**3**	**6**	**180**
S_5	—	✓	**3**	**10**	**180**
S_6	—	✓	**3**	**15**	**180**
P1		✓	**3**	**2**	**20**
P2		✓	**3**	**2**	**40**
P3		✓	**3**	**2**	**60**
P4		✓	**3**	**2**	**120**

In order to benefit from a better control of the amount of electrodeposited PbO_2 through the electrodeposition duration, galvanostatic electrodeposition (i.e. chronopotentiometry) was selected as the electrodeposition technique. Typical chronopotentiometry curves obtained for a 0.56 mA anodic current applied for 3 minutes are shown in Figure 2. Each of these curves shows the same trend: the potential increases very rapidly up to approximately 1.2-1.3 V (y-axis was cut at 1 V in Figure 2) and then decreases slowly down to approximately 0.84 V vs. AgCl/Ag, which indicates that a very good reproducibility can be achieved on condition that the surface area of the working electrode is always the same. In this potential range, anodic oxidation of Pb^{2+} cations (see reaction (1)) is the only reaction to occur as oxygen evolution was shown to

be negligible for such potential values in our experimental conditions (see Figure 2). This implies that PbO_2 is electrodeposited with a coulombic efficiency close to 100 % and by using Faraday's law, one can estimate the amount of electrodeposited PbO_2 to approximately 0.5 µmol or 0.12 mg.

Various PbO_2, PbI_2 and $CH_3NH_3PbI_3$ thin films were synthesized using the procedure described above in the experimental part as well the synthesis parameters listed in Table 1. Immediately after their synthesis, all samples were stored at dry air using a dessicator partly filled with silica gel.

2. Structural and chemical characterizations

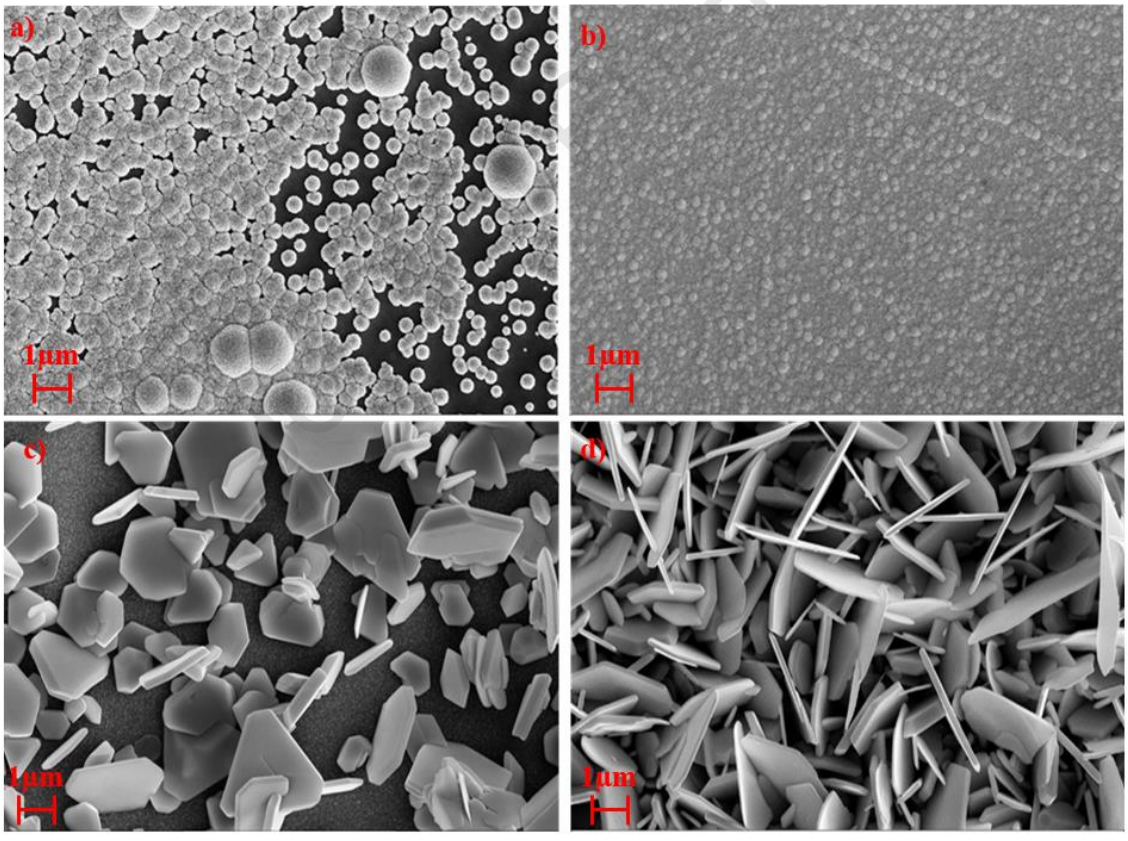

Figure 3 : SEM-FEG images of PbO_2 samples electrodeposited for 5 minutes in a) S_a, b) S_b, and of PbI_2 samples obtained after immersion in S_c for 5 minutes of a PbO_2 sample electrodeposited in c) S_a (sample D_1), d) S_b (sample D_2).

Figures 3a-b represent the surface morphology of PbO_2 thin films obtained by electrodeposition from S_a and S_b respectively. The SEM-FEG image shown in Figure 3a indicates that the PbO_2

thin film obtained in the nitrate electrolytic solution (S_a) is not totally uniform and made of grains of various size, whereas that electrodeposited from the acetate electrolytic solution (S_b) shows a continuous layer of PbO_2 particles with a narrow size distribution on the FTO substrate, in good agreement with a previous study that had already shown that acetate solution allows the electrodeposition of more uniform PbO_2 thin films [42].

These PbO_2 thin films were then converted into PbI_2 by immersion in a HI/ethanol solution (S_c) in order to produce samples D_1 and D_2 (see Table 1). Let us emphasize that such conversion occurring on supported phase is possible on condition that lead dioxide behaves as an ionic solid, and moreover it requires the reduction of lead (IV) (in PbO_2) into lead (II) (in PbI_2).

The success of this first conversion step is first confirmed by the spectacular change of i) the color of the supported layer from light brown to bright yellow, and ii) the morphology of the particles, from (hemi-)spheres for PbO_2 into well-defined platelets for PbI_2 (see SEM-FEG images on Figures 3c-d). Apart from this, PbI_2 films show features that were already visible for starting PbO_2 thin films. In particular, PbI_2 films obtained from PbO_2 electrodeposited in S_a (nitrate solution, see sample D_1 in Table 1) do not cover fully the FTO substrate and they exhibit PbI_2 particles that are not uniform in terms of size, morphology and distribution (see Figure 3c), unlike PbI_2 films obtained from PbO_2 films electrodeposited in S_b (acetate solution, see sample D_2 in Table 1) that showed well defined hexagonal platelets distributed homogeneously over the substrate surface.

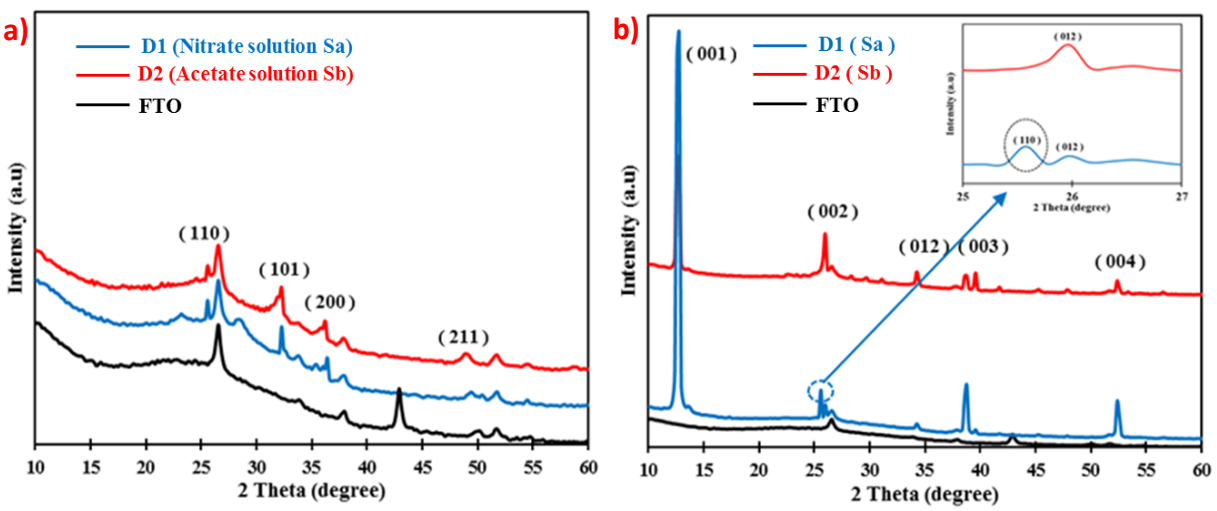

Figure 4 : X-ray diffractograms of PbO_2 samples electrodeposited for 2 minutes in a) S_a (nitrate solution), b) S_b (acetate solution), and of PbI_2 samples obtained after immersion in S_c for 5 minutes of a PbO_2 sample electrodeposited in c) S_a (nitrate solution, sample D_1), d) S_b (acetate solution, sample D_2). The Crystallography Open Database (COD) references used for the identification of β-PbO_2 and PbI_2 were 96-900-7543 and 96-900-9114 (see also JCPDS data in [43]).

The X-ray diffraction (XRD) patterns of PbO_2 films electrodeposited in S_a and S_b (see red and blue diffractograms in

Figure *4*a) both show major diffraction peaks at 25.5°, 32.2°, 36.4°, and 49.4° corresponding to (110), (101) (200), and (211) reflections of β-PbO_2 respectively [42], as well as diffraction peaks produced by the underlying FTO layer (see black diffractogram in

Figure *4*a). On

Figure *4*a, one can also observe mainly on the diffractogram of sample D1 (see blue curve) minor diffraction peaks at 23.3° and 27.6° that may correspond to (100) and (111) reflections of α-PbO_2. All together, these observations indicate therefore that both electrodeposited PbO_2 films contain mainly β-PbO_2 (rutile phase), whereas sample D1 may also contain a small portion of α-PbO_2 (orthorhombic phase) [42,43].

The diffractograms of PbI_2 samples (D_1 and D_2) (see

Figure *4*b) show sharp and strong diffraction peaks situated at 2 theta values of 12.5°, 25.9°, 34.2°, 39.5° and 52.3° and corresponding to the (001), (002), (012), (003) and (004) planes of the PbI_2 crystalline structure. However, in the case of sample D_1 obtained in S_a solution (see

blue diffractogram in Figure 4b), the plane (110) at 25.5° corresponding to β-PbO_2 was detected, indicating that PbO_2 was not fully converted to PbI_2. Nevertheless, the conversion rate of PbO_2 into Pb[illegible] some of our PbI_2 thin films (figur[illegible] 29 at.% and 33.71 at.% values for i[illegible] f 1.97 for the I/Pb atomic ratio inst[illegible]

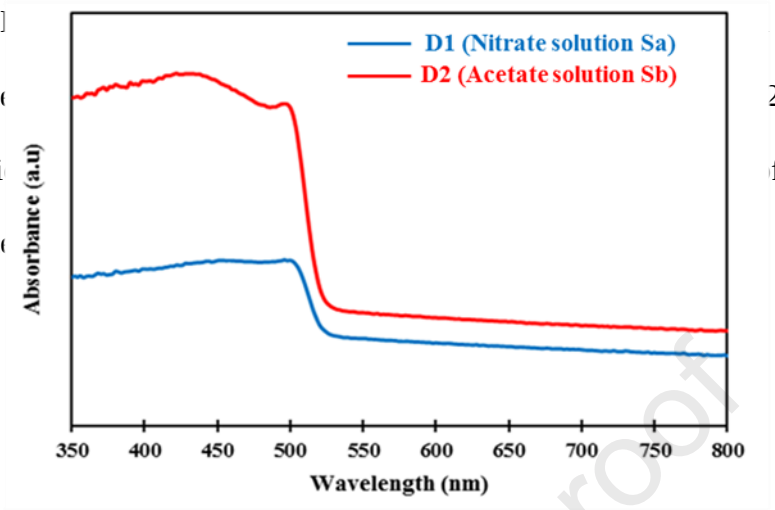

Figure 5: Absorbance spectra of PbI_2 samples (D_1 and D_2)

The conversion of PbO_2 into PbI_2 (samples D_1 and D_2) by anion exchange reaction in alcoholic solution containing HI on glass/FTO substrates was also probed by UV-visible spectroscopy. The UV-visible spectra of the PbI_2 films (see Figure 5) show an absorption onset at 515 nm, with an excitonic peak at 495 nm for the D_2 sample only, followed by a continuous absorption that extends towards the UV-region. It is remarkable here to mention that the absorbance measured for D_2 was substantially higher than that measured for D_1 all over the absorption wavelength range. Such finding highlights again that the D_2 PbI_2 sample is more attractive than the D_1 sample, knowing that it was already found to be more uniform than D_1 and almost fully free of PbO_2 in spite of an identical immersion duration in S_c.

As a consequence, as more interesting PbI_2 thin films were obtained from PbO_2 samples electrodeposited in S_b (acetate solution), the next step consisted for us in defining the optimized synthesis parameters of PbI_2 samples allowing ultimately the preparation of $CH_3NH_3PbI_3$

perovskite samples after immersion of PbI_2 samples in S_d (MAI/isopropanol solution). For this purpose, PbO_2 samples were all electrodeposited in S_b (acetate solution) with identical electrodeposition parameters (electrodeposition potential and duration). Some of them were then converted first into different PbI_2 precursor films by immersion in S_c (HI/ethanol solution) for an immersion duration ranging between 1 and 15 minutes (see samples S_1-S_6 in Table 1) and then into $CH_3NH_3PbI_3$ perovskite samples by immersion in S_d (MAI/isopropanol solution) during 180 minutes. Other identical PbO_2 samples were first immersed during 2 minutes in S_c and then during 20 to 120 minutes in S_d (see samples P_1-P_4 in Table 1). These two series of perovskite samples were aimed at studying separately the influence of the two immersion durations in S_c and S_d respectively.

The conversion of all PbO_2 films into $CH_3NH_3PbI_3$ crystal layers was confirmed by XRD regardless of the immersion times in HI (S_c) and MAI (S_d) solutions (see Figures 6a and c for S_1-S_6 and P_1-P_4 sample series respectively). This was actually evidenced by the appearance of sharp peaks at 14.2°, 20.0°, 23.6°, 24.6°, 28.5°, 31.8°, 35.0°, 40.5°, 43.2° and 50.2° that correspond to the typical tetragonal crystal structure of the perovskite in the (110), (200), (211), (202), (220), (310), (312), (224), (314) and (404) planes respectively [44,45]. However, in addition to the perovskite phase, most of the films also showed the presence of unconverted PbI_2, as revealed by a diffraction peak located at a 2 theta position of 12.5° (marked with * for S_4-S_6 and P_1-P_2 samples in Figures 6a and c). In the S1-S6 series, one can observe that, as the dipping time in HI increased, the intensities of PbI_2 reflections increased and that of the perovskite decreased, indicating that the size of the PbI_2 crystallites is increasing (see Figure 6b). Similarly, a short dipping time into MAI solution for the two samples P1 and P2 was not enough to convert all PbI_2 precursor (see Figure 6c). On the other hand, as the dipping time in MAI increased, the peak intensities and widths decreased for PbI_2, which was associated with an increase of peak intensities for the perovskite (see Figure 6d). Such observation could

indicate that the conversion mechanism starts from the surface of the PbI_2 crystallites and progresses towards their center. Therefore, the crystallinity of the $MAPbI_3$ phase increased while that of PbI_2 decreased progressively. In fact, some studies suggested that the presence of

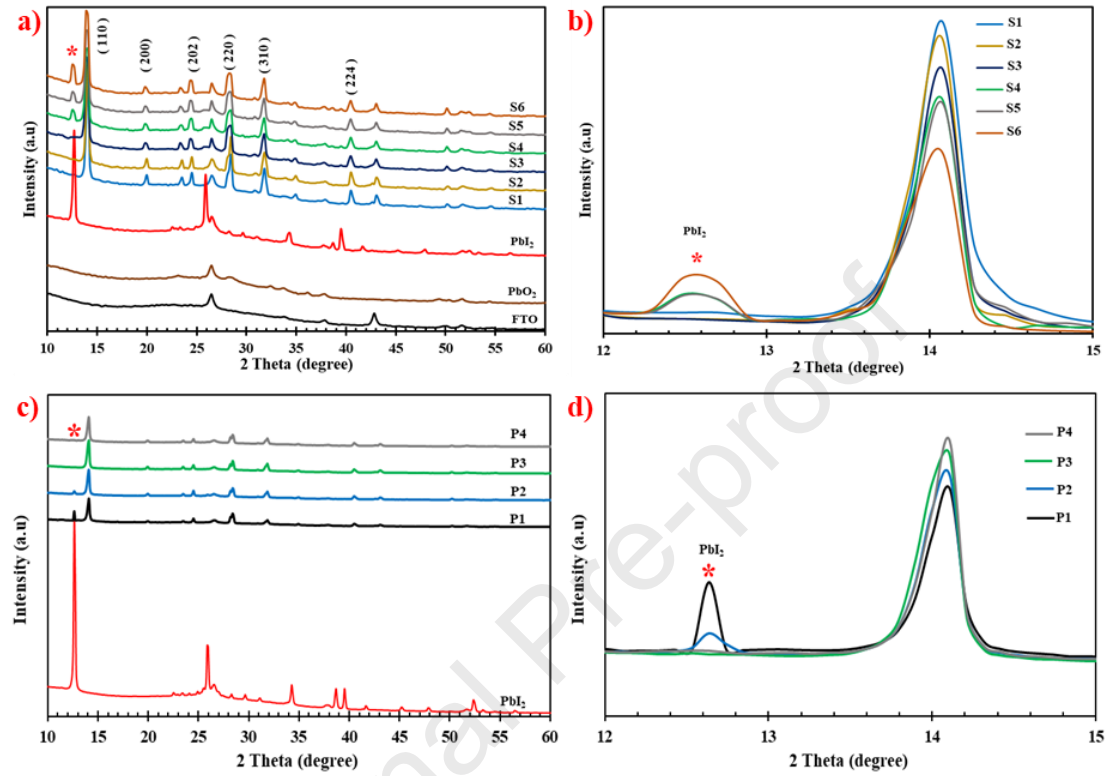

the peak representing the (001) plane of PbI_2 hexagonal 2H polytype phase was mainly due to the reminiscent PbI_2 phase in the perovskite structure [46], which indicated that thicker PbI_2 films were not fully converted into the desired $CH_3NH_3PbI_3$ perovskite [47,48].

Figure 6 : X-ray diffractograms of $CH_3NH_3PbI_3$ layers (a,b) S_1-S_6 samples, (c,d) P_1-P4 samples (see Table 1 for the different synthesis parameters).

From SEM observations, it appears that perovskite films (S_1 samples) showed a well-mastered morphology with multiple grains (see Figure 7a). As the dipping time in HI solution increased (2 minutes, see Figure 7b for sample S2), high quality perovskite cubic crystals were formed, showing a narrow size distribution and a compact layer on the underlying glass/FTO substrate. Further increase in the dipping time into HI solution (S_3 to S_6) stimulated the formation of large ensembles of crystals with arbitrary shapes.

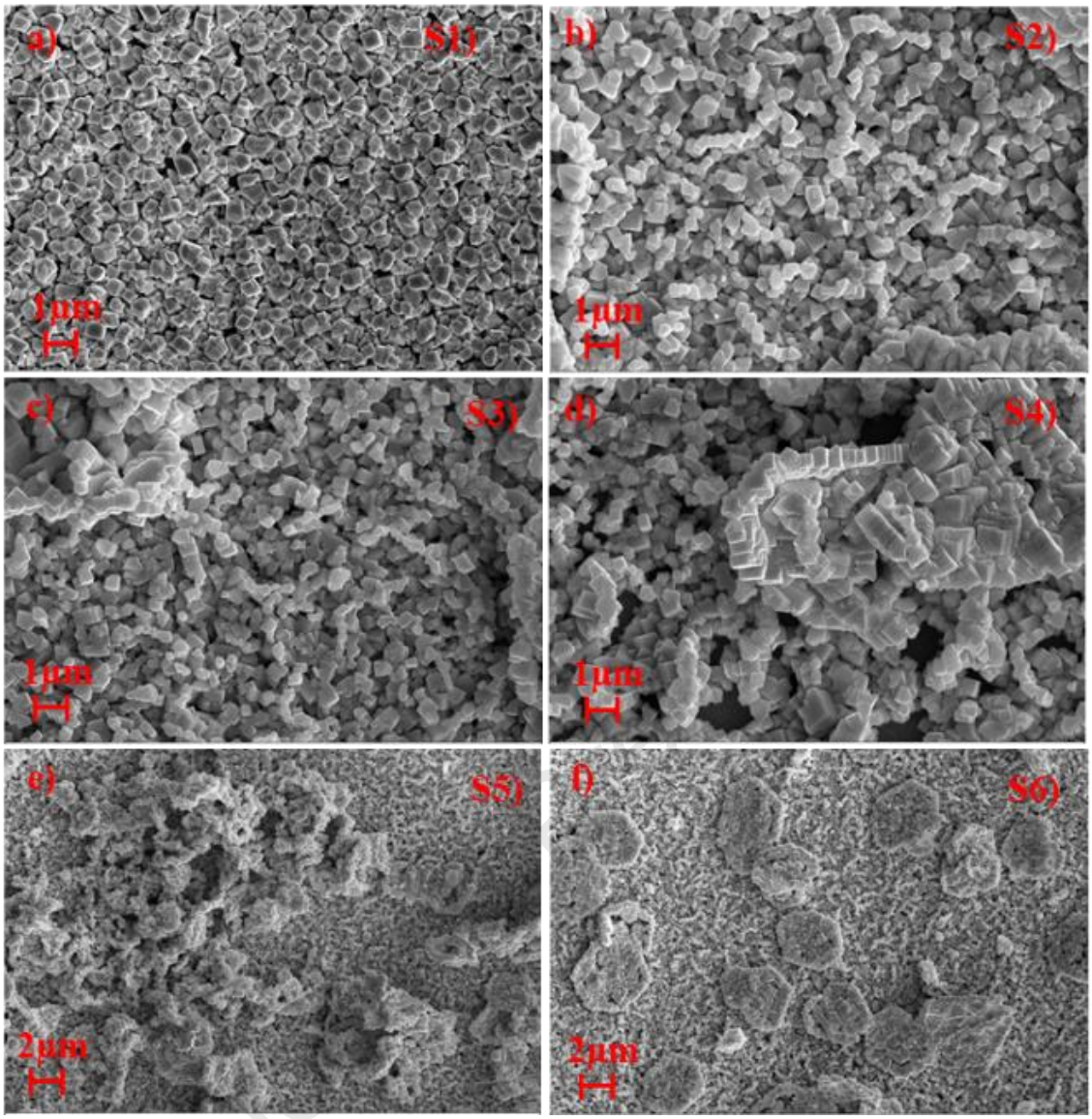

Figure 7 : SEM images of $CH_3NH_3PbI_3$ samples (S_1-S_6) obtained by immersion of PbO_2 samples first during different immersion times in S_c (HI/ethanol solution), and then for 3 hours in S_d (MAI/isopropanol solution).

Beyond the surprising role of dipping time of identical PbI_2 samples in MAI solution on the morphology of resulting S1-S6 perovskite samples, the influence of the immersion time of identical PbO_2 samples in S_c (HI/ethanol solution) was also explored (see Figure 8). A very dense distribution of mainly vertical PbI_2 platelets oriented randomly is observed in Figure 8a.

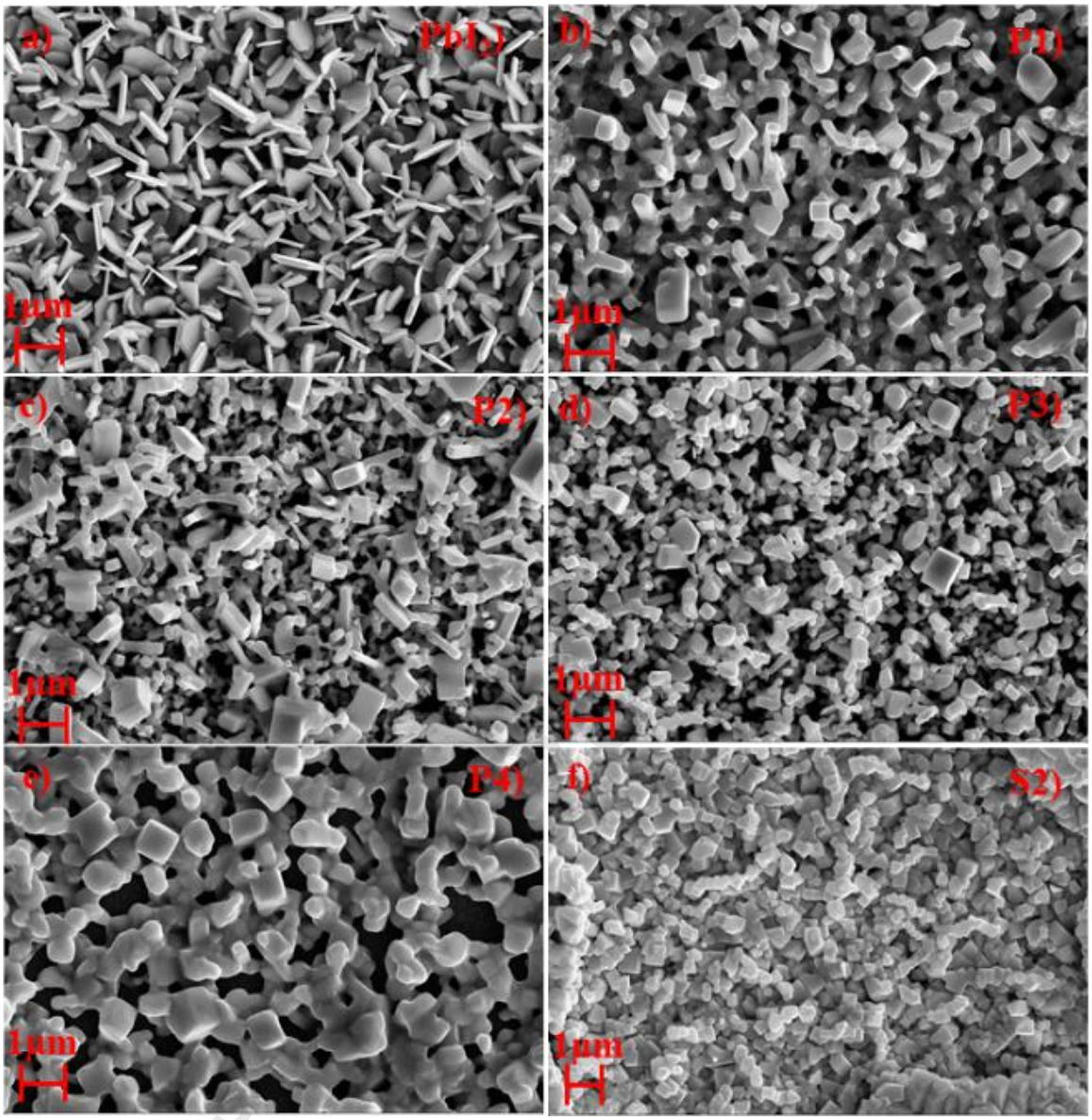

Figure 8 : SEM images of a) PbI_2, b-f) $CH_3NH_3PbI_3$ samples obtained by immersion of PbO_2 samples, b-e) first during 2 minutes in S_c (HI/ethanol solution), and then during different immersion times in S_d (MAI/isopropanol solution)(see samples P_1-P_4 in Table 1), and f) first during 2 minutes in S_c (HI/ethanol solution), and then during 180 minutes in S_d (MAI/isopropanol solution)(see S_2 in Table 1, this latter sample is expected to be a PbI_2 free perovskite according to its diffractogram shown in Figure 6a).

Visually, when the dipping time in MAI was set between 20 and 40 min (see samples P_1 and P_2 in Figure 8b-c), small lead iodide platelets were still present in the resulting layers, beside a fair amount of cubic crystals of perovskite, indicating that the conversion of PbI_2 platelets into well-shaped cubic crystals of perovskite was on its way, i.e. not complete. Such observation fully supports the XRD results shown in Figure 6c and commented above concerning the remaining PbI_2 at lower immersion times in MAI. As the dipping time increased up to 60 and 120 minutes

(see samples P3-P4 in Figure 8d-e), the platelet structures disappeared gradually. When the dipping time increased to 180 minutes (see sample S_2 in Figure 8f), a dense and homogeneous distribution of $CH_3NH_3PbI_3$ crystals and a lower density of pinholes appeared, as a consequence of the formation of smaller perovskite cubic crystals.

In order to quantify the amount of lead and iodide present in ours samples, EDS analysis was performed (see Figure 9). The I/Pb ratio for pure PbI_2 is 2, whereas it is 3 for pure perovskite, i.e. without further PbI_2 impurities. As shown in Figure 9a, the I/Pb atomic ratio decreased gradually from 2.93 to 2.87, when the dipping time in HI solution increased from 1 to 15 mn. This indicates that a longer dipping time in HI solution does not allow the full conversion of PbI_2 platelets to cubic perovskite crystals and PbI_2 was still present as suggested by the XRD analysis reported above. On the contrary, longer dipping times in MAI solution do lead to an increase of the I/Pb ratio, which indicates that the PbI_2 crystals were converted gradually to perovskite crystals, as already observed from XRD and SEM analysis.

According to the SEM results, we did notice the morphological changes from platelets to cubes passing through an intermediate state between the two, and we suggest that PbI_2 re-dissolves in MAI solutions and recrystallizes into perovskite cubes, or the step between the PbI_2 platelet and the perovskite cubes is amorphous so it is not detected by XRD.

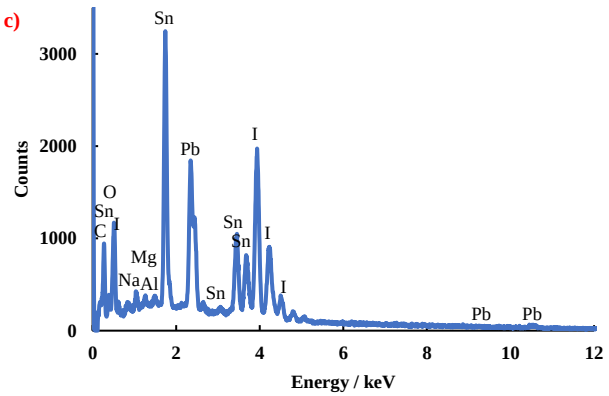

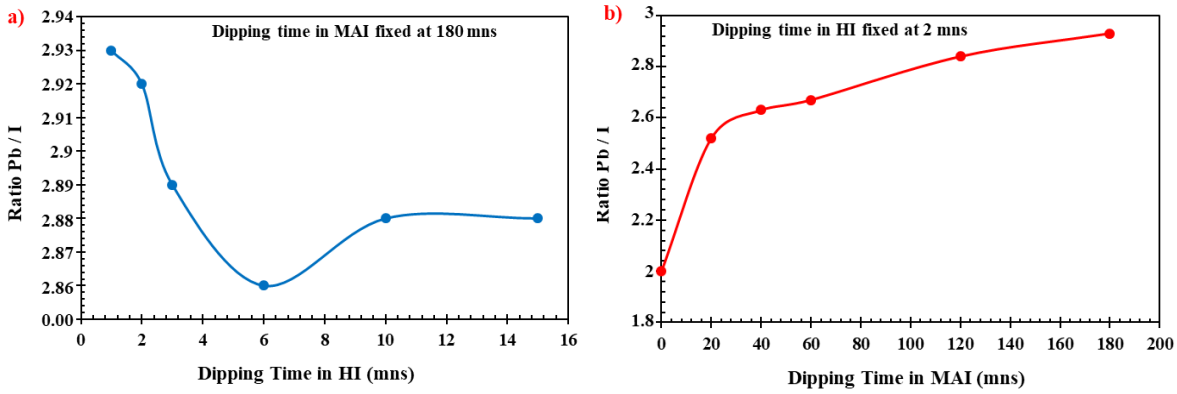

Figure 9: Ratio of lead/iodide (Pb/I) as function of the dipping time a) in MAI solutions at a fixed dipping time in HI (2 minutes, see samples S_1-S_6 in Table 1), b) in HI solutions at a fixed dipping time in MAI (180 minutes, see samples PbI_2 (no dipping in MAI solution), S_2 and P_1- P_4 in Table 1). c) typical EDS spectrum of a perovskite thin film deposited on a glass/indium tin oxide substrate. Pb : 72.77, I : 27.23 in at.% (other elements were not integrated in the at.% calculations).

From these EDS results concerning the atomic percentages of lead and iodine in the final perovskite layers, the percentages of PbI_2 and perovskite entities in the perovskite films were calculated as a function of the dipping time in HI and MAI solutions by building and solving a two equation system involving n*(PbI₂)* and n*(perovskite)* as two unknown parameters :

$$n(PbI_2) + n(perovskite) = n_{at}(Pb) \quad (2) \qquad \text{and} \qquad 2n(PbI_2) + 3n(perovskite) = n_{at}(I) \quad (3)$$

In these two equations, n*(PbI₂)* and n*(perovskite)* represent the number of moles of PbI_2 and $CH_3NH_3PbI_3$ entities in a given perovskite layer respectively, whereas $n_{at}(Pb)$ and $n_{at}(I)$ represent the number of moles of Pb and I atoms, both as extracted from EDS analysis for this same perovskite layer.

The results illustrated in Figure 10a show that with an increase of dipping time in HI solution and a constant dipping time in MAI (180 mn), the percentage of PbI_2 detected in the perovskite layer increases from 0% for a dipping time of 0 mn to almost 12% for dipping times varying between 3 and 15 min. In Figure 10b, the PbI_2 % decreases from 100% for a PbI_2 film resulting from dipping of a PbO_2 film during two minutes in a HI solution (without any dipping in the MAI solution) to 6% for a perovskite film obtained from dipping of a PbO_2 film first during two minutes in a HI solution and then during a maximum dipping time of 180 min in a

MAI solution. These results indicate that PbI_2 is always present in the final perovskite layer with a percentage that depends on both immersion durations in HI and MAI solutions, and is only detected by XRD for PbI_2 percentages higher than 22%, as a consequence of its limit of

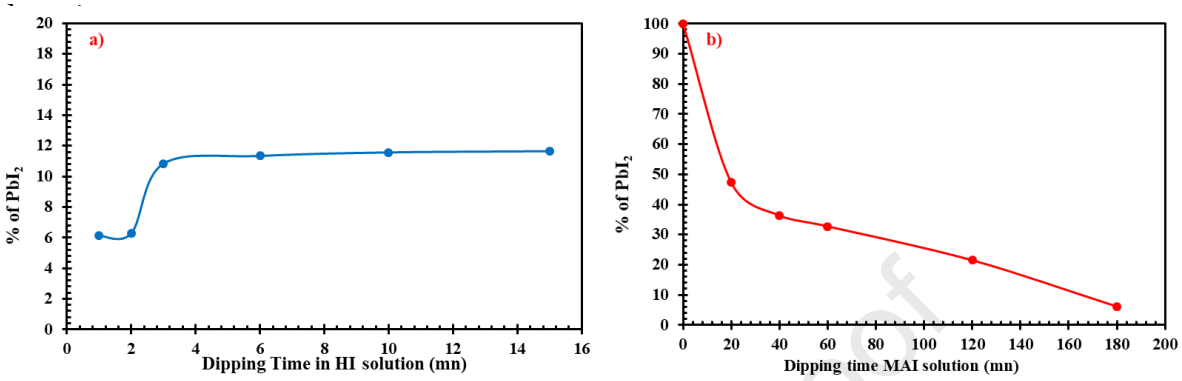

Figure 10 : Percentage of PbI_2 entities in the perovskite layer as a function of : a) immersion time in HI alcoholic solution (S_1-S_6 samples), b) immersion time in MAI alcoholic solution (PbI_2, P_1-P_4, and S_2 samples).

3. Opto-electronic characterizations

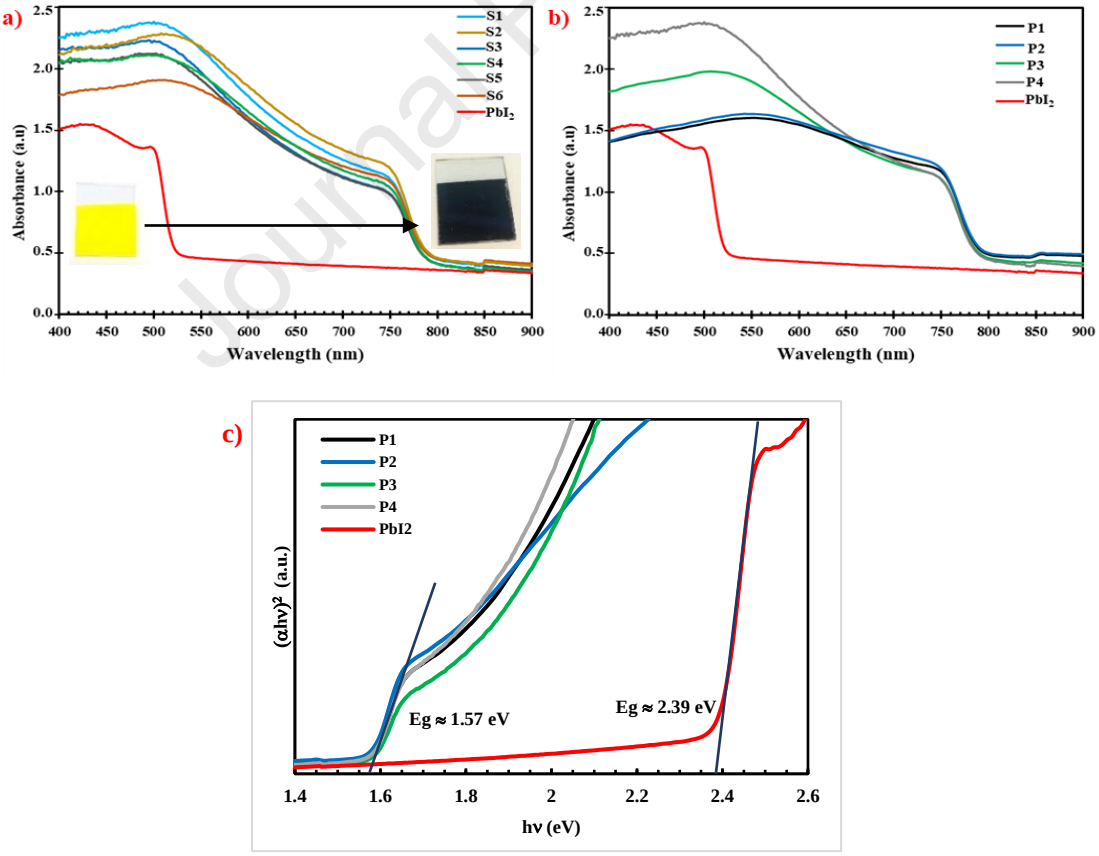

Figure 11 : a) Absorption spectra of the PbI_2 and perovskite films synthesized at different immersion times in HI (see samples S_1-S_6 in Table 1), b) Absorption spectra of the PbI_2 and perovskite films synthesized at different immersion times in MAI (see Table 1), c) Tauc plots for PbI_2 and perovskites samples produced in this work.

The optical band gaps of PbI_2 and perovskite films synthesized in this work were determined by constructing Tauc plots from UV-vis spectra obtained for each of these samples. Let us remind that Tauc equation can be written as follows:

$$(\alpha h\nu)^{1/n} = A\,(h\nu - Eg) \qquad (4)$$

In this equation, n = 1/2 for direct optical transitions, and α, hν, and E_g are the absorption coefficient, photon energy, and the optical bandgap energy of the investigated layer, respectively [49].

As shown in Figure 11, for all the perovskite samples (see samples S_1-S_6 in Figure 11a as well as samples P_1-P_4 in Figure 11b), the corresponding absorbance spectra are very similar and an intense absorbance was measured for each of them all over the visible range, which is not the case for a PbI_2 sample (see red curve in Figure 11a). The absorption edge wavelength undergoes a massive shift, increasing from 510-530 nm for PbI_2 to 760-780 nm for all the perovskite samples, testifying thus to the successful chemical conversion of PbI_2 layer into a $CH_3NH_3PbI_3$ perovskite film and the structural transition detected by XRD measurements. It appears therefore from Figure 11a that the onset of absorption does not change with the immersion duration of the PbO_2 samples in S_c (HI/ethanol solution). The evolution of these spectra with reaction time is in good agreement with a change of color of the samples, which turns from bright yellow for crystalline PbI_2 to dark brown for $MAPbI_3$, as shown in the inset pictures of

Figure 11a.

Moreover, all the spectra are shifted upwards possibly due to the effects of light scattering caused by the formation of large crystals of perovskite. The estimated optical bandgaps of all the fabricated $CH_3NH_3PbI_3$ layers (S_1-S_6 as well as P_1-P_4) were all found to be very close to 1.55 eV, the bandgap value usually reported in literature for the $CH_3NH_3PbI_3$ perovskite [46], and therefore very different from the one determined for PbI_2 thin films, i.e. 2.39 eV.

Mott-Schottky (MS) measurements were performed so as to determine the capacitance of each of the perovskite samples (S_1-S_6 and P_1-P_4). Resulting MS plots, i.e. plots of $1/C^2$ vs applied potential at different frequencies were found to be in good agreement with the Mott-Schottky equation (see Figure 12 for sample S_4). This latter establishes a simple relation between the capacitance of a space charge layer and the flat-band potential (E_{FB}) also called built-in potential:

$$\frac{1}{C^2} = \frac{2}{A^2 q \varepsilon \varepsilon_0 N_D}\left[(E_{FB} - E) - \frac{kT}{q}\right] \quad (5)$$

where C is the interfacial capacitance (i.e., capacitance of the semiconductor depletion layer, in Farad (F)), ε is the dielectric constant of $CH_3NH_3PbI_3$ (taken as 6.5)[21], ε_0 is the permittivity of vacuum (8.85 10^{-14} $F.cm^{-1}$), A is the surface area (1.5 cm^2 in our experimental conditions), N_D is the doping density (also called carrier density, in cm^{-3}) of donors/acceptors in the semiconductor which are important parameters to describe a semiconductor/electrolyte

interface, E is the applied potential, E_{FB} is the flat band potential (or built-in potential) when a semiconductor electrode is brought in contact with an electrolyte solution, T is the absolute temperature (298 K), k is the Boltzmann constant (1.38 10^{-23} $J.K^{-1}$) and q is the electron charge (1.6 x 10^{-19} C). The temperature term is generally small and can be neglected (at room temperature, kT/q in equation (5) is 0.026 V).

Figure 12 : a) Mott-Schottky plots of a $CH_3NH_3PbI_3$ sample (S_4) in 0.1 M $TBAPF_6/CH_2Cl_2$ electrolyte at different frequencies.

As shown in Figure 12, the MS plots of a thick $CH_3NH_3PbI_3$ film (S_4) (thickness > 1 µm) were obtained at various frequencies. They all show a linear dependence of $1/C^{-2}$ term with the applied potential over approximately the same potential range, i.e. from 0.64 to 0.95 V vs. Ag^+(10 mM)/Ag in CH_3CN, that is lost for potential values lower than 0.64 V vs. Ag^+(10 mM)/Ag in CH_3CN. From the exploitation of the intercepts of the linear portion of these MS plots with the x-axis (potential axis), flat-band potential values were extracted for different frequency values (see Table 2). They appear to be in good agreement with those published in literature [50]. It is interesting to observe from data reported in literature that the E_{FB} values of perovskite thin films depend on the synthesis method. For example, E_{FB} of spin coated $CH_3NH_3PbI_3$ is 0.67 V vs. Ag^+(10 mM)/Ag in CH_3CN (same reference electrode as ours) [21,51]. Even though E_{FB} was found to vary with the frequency for a given perovskite sample, no obvious dependence was observed in our experimental conditions, which could suggest that the same value, i.e. 0.95 ± 0.05 V vs. Ag^+(10 mM)/Ag in CH_3CN is always measured with a

little uncertainty. The C^{-2} plot shows perturbations around 0.45 V vs. Ag^{+}(10 mM)/Ag in CH_3CN that have also been detected in thin films deposited on conducting oxide substrates. They are considered as an indication that the depletion region has extended to the substrate with the applied potential [52]. The Mott-Schottky plot shown in Figure 12 exhibits a linear behavior with a negative slope over a large potential range until the flat-band value (E_{FB}). This behavior is consistent with an ideal semiconductor/electrolyte junction, and the sign of the slope of this MS plot is clearly consistent with a p-type semiconductor. Carrier density (N_A) can be determined from the slope (S) of the MS plot for different frequency values (see Table 2) by using the following equation:

Table 2 : $CH_3NH_3PbI_3$ semi-conducting perovskite / electrolyte interface characteristics obtained from Mott-Schottky plots for different frequencies for sample S_4 (see Table 1).

Frequency (kHz)	***V_{FB} (V / Ag^{+}(10 mM)/Ag in CH_3CN)***	***N_D (cm^{-3})***
0.5	**0.94**	**2.75×10^{20}**
1	**0.94**	**2.70×10^{20}**
2	**0.9**	**4.41×10^{20}**
5	**1**	**1.10×10^{20}**

$$|S| = 2 / (q\varepsilon_0\varepsilon_r N_A) \quad (6)$$

The obtained values are all close to 10^{20} cm^{-3}, and therefore rather higher than those reported previously in literature [51,53,54], and they were not found to vary significantly with the synthesis parameters used in this work for the samples S_1-S_6.

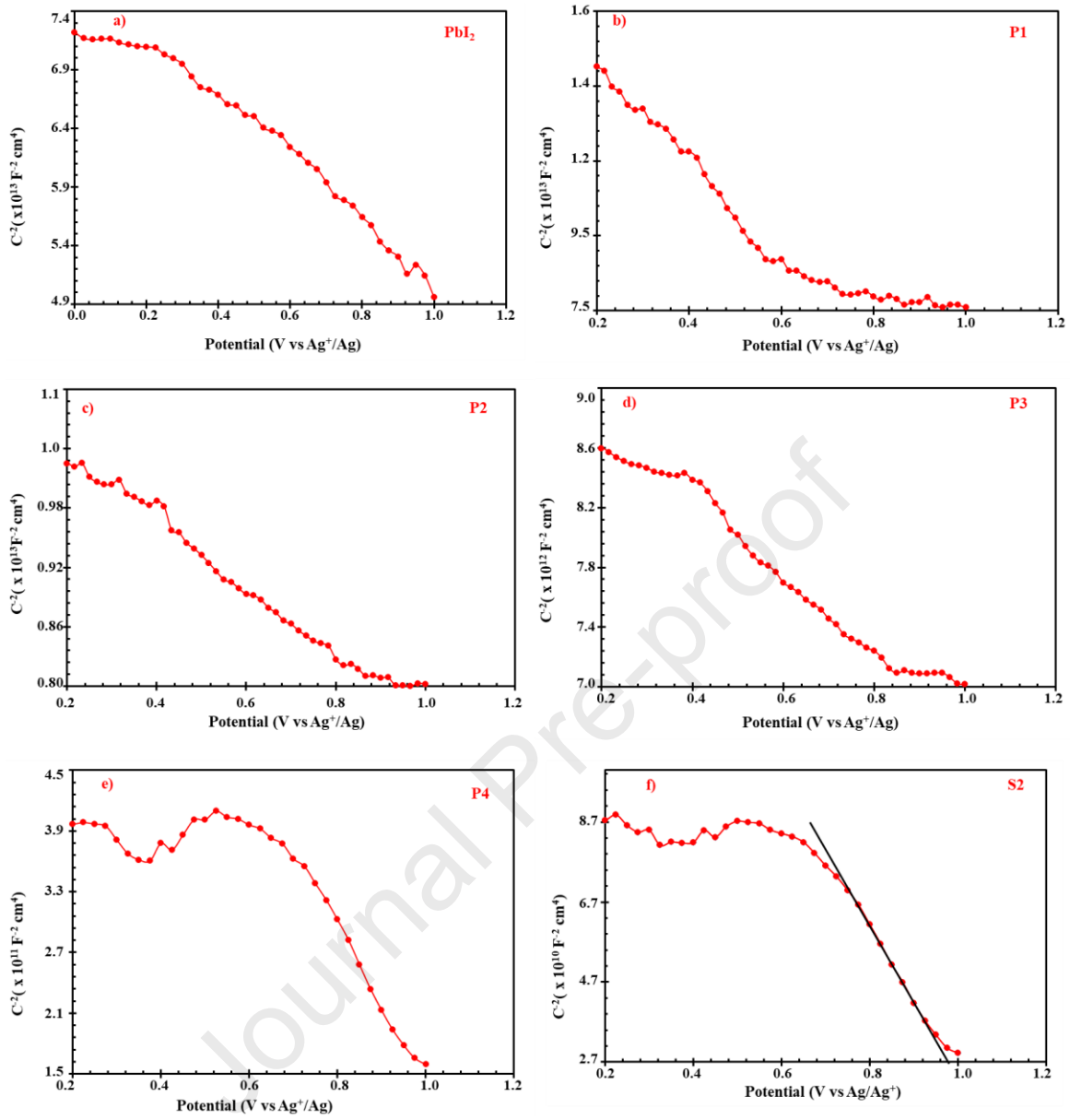

Figure 13: a-e) Mott-Schottky plots of $CH_3NH_3PbI_3$ samples (P_1-P_4 and S_2) in 0.1 M $TBAPF_6/CH_2Cl_2$ electrolyte at 2 kHz, f) Mott-Schottky plots of $CH_3NH_3PbI_3$ (S_4 sample) measured at 2 kHz and linear extrapolation of the linear part of the curve allowing the determination of the flat-band potential.

Since the exploitation of MS plots of S_1-S_6 samples did not reveal any variation in carrier density at different frequencies, MS plots of PbI_2 and perovskites (P_1-P_4) immersed at different times in the MAI at a fixed frequency of 5 kHz were performed (see Figure 13). The MS slope showed again a negative slope corresponding to a p-type perovskite for all P_1-P_4 samples. The capacitance of the layers decreased from 10^{13} F for the PbI_2 layer (see Figure 13a) to 10^{10} F as the dipping time in MAI increases, while it was mainly constant for the S_1-S_6 series as a function

of the dipping in HI (10^{10} F). This resulted in an increase in carrier density from 10^{17} for PbI_2 to 10^{20} cm^{-3} (see samples P_1-P_4 and S_2 in Table 3).

Table 3: $CH_3NH_3PbI_3$ semi-conducting perovskite / electrolyte interface characteristics obtained from Mott-Schottky plots at 2 kHz for all samples immersed in MAI.

Samples	***V_{FB}*** ***(V / Ag^+(10 mM)/Ag in CH_3CN)***	***N_A (cm^{-3})***
PbI_2	**0.99**	**1.04×10^{17}**
P_1	**0.62**	**5.54×10^{17}**
P_2	**0.81**	**4.42×10^{18}**
P_3	**0.88**	**7.04×10^{18}**
P_4	**0.95**	**2.20×10^{19}**
S_2	**0.97**	**1.06×10^{20}**

At this stage, the carrier density values calculated for the perovskite (S_1-S_6 and P_1-P_4) and PbI_2 samples (see Table 3) can be discussed as a function of the PbI_2 % values determined from EDS measurements and plotted in Figure 10 as a function of the immersion times in HI or MAI solutions. As far as the S_1-S_6 samples are concerned, the percentage of PbI_2 varies between 6 and 12% (see Figure 10a) while the carrier density remains unchanged and always of the order of 10^{20} cm^{-3}. One can say in other words that whatever the percentage of PbI_2 between 6 and 12%, these perovskite films all behave as highly doped p-type semiconductors and no influence of dipping time in HI was observed, knowing that the dipping time in MAI solution was always fixed at 180 minutes for this series of samples. On the other hand, as shown in Figure 10b for samples whose dipping time in HI solution was 2 mn, the percentage of PbI_2 decreases as the dipping time in MAI increases and the carrier density increases from 10^{17} to 10^{20} cm^{-3} (see Table 3). It is remarkable here that the carrier density of PbI_2 is initialy 10^{17} cm^{-3}, and from the time the PbI_2 layer is dipped in MAI solution, it turns into a perovskite layer containing a certain percentage of PbI_2 varying between 100 and 6 % which controls the final carrier density. For

illustration, a perovskite film obtained after a 20 minutes immersion of PbI_2 in MAI solution still contains 47.2% of PbI_2 and its carrier density is only slightly higher than that of PbI_2 (5.54 10^{17} cm^{-3} instead of about 10^{17} cm^{-3} for PbI_2). As the dipping time increases to 40 and then 60 minutes, the PbI_2 % decreases down to 36 and 32% respectively whereas the carrier density of these perovskite films increases up to 4.42 and 7.04 10^{18} cm^{-3}. Finally, with increasing the dipping time in MAI up to 120 and 180 minutes, the resulting perovskite films both contain a low PbI_2 fraction, i.e. 21 and 6% respectively while the carrier density reaches high values, close to 10^{19} and 10^{20} cm^{-3} respectively. It appears therefore that, for a fixed dipping time in HI (i.e. 2 minutes in our experimental conditions), the lower the percentage of PbI_2 in the perovskite film, the higher the carrier density of this latter. Therefore, the parameter controlling the carrier density of our perovskite samples in this case is the dipping time in the MAI alcoholic solution which in turn influences the remaining percentage of PbI_2. In other words, the properties (carrier density in particular) of electrodeposited perovskite layers can be adjusted according to the desired application so that they can have low or high carrier densities.

Conclusion

Perovskite $CH_3NH_3PbI_3$ thin films have been synthesized by using a very simple synthesis method involving only an electrodeposition step combined with two consecutive chemical conversion steps that were carried out by immersion in two different alcoholic solutions containing respectively HI and MAI. Whatever the two immersion durations, the resulting perovskite thin films all show a p-type semiconductor behavior, as indicated by the negative slope of Mott-Schottky plots and their optical bandgap is very close to 1.57 eV and therefore quite different from the one of PbI_2 (2.39 eV), even though XRD and SEM-FEG/EDS analyses allowed us to detect and quantify PbI_2 impurities in our perovskite layers. By comparing the PbI_2 % in our perovskite layers with their carrier density, extracted as well from our Mott-Schottky measurements, we clearly demonstrate that they vary in opposite directions. When the

PbI_2 % decreases from 48 % down to 6%, the carrier concentration increases from 5.54 10^{17} cm^{-3} up to 1.06 10^{20} cm^{-3}, a value corresponding to a highly doped perovskite layer. With such observations, we provide a better understanding of the influence of PbI_2 impurities on the carrier density of electrodeposited perovskite layers. We also amplify the attractiveness of our synthesis method, electrodeposition combined with two conversion steps by simple immersion, by showing that the carrier concentration can be tuned on purpose inside a large range. This makes this synthesis method very interesting promising for the large scale production of p-type semiconducting perovskite thin films.

Acknowledgements

Dr L. Fillaud (LISE laboratory, Sorbonne University) is warmly acknowledged for her precious help in the synthesis and purification of methylammonium iodide (MAI or CH_3NH_3I) salt.

Bibliography

[1] R. Gupta, R. Datt, S. Barthwal, H. Sharma, A. Pandey, R. Deka, P. Sarkar, S. Husale, R. Srivastava, V. Gupta, S. Arya, S. Pathak, Synthesis and characterization of all-inorganic (CsPbBr3) perovskite single crystals, Mater. Adv. 3 (2022) 7865–7871. https://doi.org/10.1039/d2ma00345g.

[2] R. Gupta, V. Gupta, R. Datt, S. Arya, A. Pandey, A. Singh, S. Husale, R. Srivastava, S. Pathak, Enhanced photosensitive properties of a single-crystal formamidinium lead bromide iodine (FAPbBr2I) based photodetector, Mater. Adv. 3 (2022) 2089–2095. https://doi.org/10.1039/d1ma01096d.

[3] M.A. Green, E.D. Dunlop, D.H. Levi, J. Hohl-Ebinger, M. Yoshita, A.W.Y. Ho-Baillie, Solar cell efficiency tables (version 54), Prog. Photovoltaics Res. Appl. 27 (2019) 565–575. https://doi.org/10.1002/pip.3171.

[4] R. Datt, S. Bishnoi, H.K.H. Lee, S. Arya, S. Gupta, V. Gupta, W.C. Tsoi, Down-conversion materials for organic solar cells: Progress, challenges, and perspectives, Aggregate. 3 (2022) 1–21. https://doi.org/10.1002/agt2.185.

[5] A. Kojima, K. Teshima, Y. Shirai, T. Miyasaka, Organometal halide perovskites as visible-light sensitizers for photovoltaic cells, J. Am. Chem. Soc. 131 (2009) 6050–6051. https://doi.org/10.1021/ja809598r.

[6] M. Kim, G.H. Kim, T.K. Lee, I.W. Choi, H.W. Choi, Y. Jo, Y.J. Yoon, J.W. Kim, J. Lee, D. Huh, H. Lee, S.K. Kwak, J.Y. Kim, D.S. Kim, Methylammonium Chloride Induces Intermediate Phase Stabilization for Efficient Perovskite Solar Cells, Joule. 3 (2019) 2179–2192. https://doi.org/10.1016/j.joule.2019.06.014.

[7] H. Zhang, H. Xu, X. Ji, J. Liang, Q. Yu, Progress toward Applications of Perovskite Solar Cells, Energy and Fuels. 34 (2020) 6624–6633. https://doi.org/10.1021/acs.energyfuels.0c00485.

[8] A.K. Jena, A. Kulkarni, T. Miyasaka, Halide Perovskite Photovoltaics: Background, Status, and Future Prospects, Chem. Rev. 119 (2019) 3036–3103. https://doi.org/10.1021/acs.chemrev.8b00539.

[9] G.E. Eperon, S.D. Stranks, C. Menelaou, M.B. Johnston, L.M. Herz, H.J. Snaith, Formamidinium lead trihalide: A broadly tunable perovskite for efficient planar heterojunction solar cells, Energy Environ. Sci. 7 (2014) 982–988. https://doi.org/10.1039/c3ee43822h.

[10] F. Khelfaoui, I. Belaidi, N. Attaf, M.S. Aida, Effect of film structure on CH3NH3PbI3 perovskite thin films' degradation, AIP Adv. 11 (2021). https://doi.org/10.1063/5.0030610.

[11] G. Saleh, G. Biffi, F. Di Stasio, B. Martín-García, A.L. Abdelhady, L. Manna, R. Krahne, S. Artyukhin, Methylammonium Governs Structural and Optical Properties of

Hybrid Lead Halide Perovskites through Dynamic Hydrogen Bonding, Chem. Mater. (2021). https://doi.org/10.1021/acs.chemmater.1c03035.

[12] H. Li, Q. Wang, H. Li, J. Zhuang, H. Guo, X. Liu, H. Wang, R. Zheng, X. Gong, Interface Modification for Enhanced Efficiency and Stability Perovskite Solar Cells, J. Phys. Chem. C. 124 (2020) 12948–12955. https://doi.org/10.1021/acs.jpcc.0c02628.

[13] C.C. Boyd, R. Cheacharoen, T. Leijtens, M.D. McGehee, Understanding Degradation Mechanisms and Improving Stability of Perovskite Photovoltaics, Chem. Rev. 119 (2019) 3418–3451. https://doi.org/10.1021/acs.chemrev.8b00336.

[14] P. Mahajan, B. Padha, S. Verma, V. Gupta, R. Datt, W.C. Tsoi, S. Satapathi, S. Arya, Review of current progress in hole-transporting materials for perovskite solar cells, J. Energy Chem. 68 (2022) 330–386. https://doi.org/10.1016/j.jechem.2021.12.003.

[15] T. Zhu, Y. Yang, X. Gong, Recent Advancements and Challenges for Low-Toxicity Perovskite Materials, ACS Appl. Mater. Interfaces. 12 (2020) 26776–26811. https://doi.org/10.1021/acsami.0c02575.

[16] Q. Wang, Y. Shao, H. Xie, L. Lyu, X. Liu, Y. Gao, J. Huang, Qualifying composition dependent p and n self-doping in CH3NH3PbI3, Appl. Phys. Lett. 105 (2014). https://doi.org/10.1063/1.4899051.

[17] J. Kim, S.H. Lee, J.H. Lee, K.H. Hong, The role of intrinsic defects in methylammonium lead iodide perovskite, J. Phys. Chem. Lett. 5 (2014) 1312–1317. https://doi.org/10.1021/jz500370k.

[18] Z. Chen, P. He, D. Wu, C. Chen, M. Mujahid, Y. Li, Processing and Preparation Method for High-Quality Opto-Electronic Perovskite Film, 8 (2021) 1–13. https://doi.org/10.3389/fmats.2021.723169.

[19] M. Liu, M.B. Johnston, H.J. Snaith, Efficient planar heterojunction perovskite solar cells by vapour deposition, Nature. 501 (2013) 395–398.

https://doi.org/10.1038/nature12509.

[20] P. Luo, Z. Liu, W. Xia, C. Yuan, J. Cheng, Y. Lu, A simple in situ tubular chemical vapor deposition processing of large-scale efficient perovskite solar cells and the research on their novel roll-over phenomenon in J-V curves, J. Mater. Chem. A. 3 (2015) 12443–12451. https://doi.org/10.1039/c5ta02306h.

[21] Z. Li, C.C. Mercado, M. Yang, E. Palay, K. Zhu, Electrochemical impedance analysis of perovskite-electrolyte interfaces, Chem. Commun. 53 (2017) 2467–2470. https://doi.org/10.1039/c6cc10315d.

[22] D. Liu, J. Yang, T.L. Kelly, Compact layer free perovskite solar cells with 13.5% efficiency, J. Am. Chem. Soc. 136 (2014) 17116–17122. https://doi.org/10.1021/ja508758k.

[23] I. Belaidi, F. Khelfaoui, N. Attaf, A. Azzizi, M.S. Aida, Solvent and Spinning Speed Effects on CH3NH3PbI3 Films Deposited by Spin Coating, Phys. Status Solidi Appl. Mater. Sci. 216 (2019) 1–9. https://doi.org/10.1002/pssa.201900340.

[24] B.R. Sutherland, S. Hoogland, M.M. Adachi, C.T.O. Wong, E.H. Sargent, Conformal organohalide perovskites enable lasing on spherical resonators, ACS Nano. 8 (2014) 10947–10952. https://doi.org/10.1021/nn504856g.

[25] A.T. Barrows, A.J. Pearson, C.K. Kwak, A.D.F. Dunbar, A.R. Buckley, D.G. Lidzey, Efficient planar heterojunction mixed-halide perovskite solar cells deposited via spray-deposition, Energy Environ. Sci. 7 (2014) 2944–2950. https://doi.org/10.1039/c4ee01546k.

[26] H. Back, G. Kim, J. Kim, J. Kong, T.K. Kim, H. Kang, H. Kim, J. Lee, S. Lee, K. Lee, Achieving long-term stable perovskite solar cells: Via ion neutralization, Energy Environ. Sci. 9 (2016) 1258–1263. https://doi.org/10.1039/c6ee00612d.

[27] M. Buda, J. Moutet, A. Pailleret, E. Saint-aman, Electrosynthesis and coordination

chemistry of poly (ferrocene bipyridyl) films, J. Electroanal. Chem. 484 (2000) 164–171. https://doi.org/10.1016/S0022-0728(00)00073-5.

[28] L.T.T. Kim, C. Gabrielli, A. Pailleret, H. Perrot, Correlation between ion-exchange properties and swelling/shrinking processes in hexasulfonated calix[6]arene doped polypyrrole films: Ac-electrogravimetry and electrochemical atomic force microscopy investigations, Electrochim. Acta. 56 (2011) 3516–3525. https://doi.org/10.1016/j.electacta.2010.11.066.

[29] N.J. Gimble, K. Nieto, A.L. Prieto, Electrodeposition as a powerful tool for the fabrication and characterization of next-generation anodes for sodium ion rechargeable batteries, Electrochem. Soc. Interface. 30 (2021) 59–63. https://doi.org/10.1149/2.F09211IF.

[30] R.N. Bhattacharya, CIGS-based solar Cells prepared from electrodeposited stacked Cu/In/Ga Layers, Sol. Energy Mater. Sol. Cells. 113 (2013) 96–99. https://doi.org/10.1016/j.solmat.2013.01.028.

[31] C. Janáky, K. Rajeshwar, The role of (photo)electrochemistry in the rational design of hybrid conducting polymer/semiconductor assemblies: From fundamental concepts to practical applications, Prog. Polym. Sci. 43 (2015) 96–135. https://doi.org/10.1016/j.progpolymsci.2014.10.003.

[32] C. Benmouhoub, J. Agrisuelas, N. Benbrahim, F. Pillier, C. Gabrielli, A. Kadri, A. Pailleret, H. Perrot, O. Sel, Influence of the incorporation of CeO2 nanoparticles on the ion exchange behavior of dodecylsulfate doped polypyrrole films: Ac-electrogravimetry investigations, Electrochim. Acta. 145 (2014) 270–280. https://doi.org/10.1016/j.electacta.2014.07.151.

[33] E. Ngaboyamahina, C. Debiemme-Chouvy, A. Pailleret, E.M.M. Sutter, Electrodeposition of Polypyrrole in TiO<inf>2</inf> Nanotube Arrays by Pulsed-Light

and Pulsed-Potential Methods, J. Phys. Chem. C. 118 (2014) 26341–26350. https://doi.org/10.1021/jp507491x.

[34] A. Pailleret, N.T.L. Hien, D.T.M. Thanh, C. Deslouis, Surface reactivity of polypyrrole/iron-oxide nanoparticles: Electrochemical and CS-AFM investigations, in: J. Solid State Electrochem., 2007: pp. 1013–1021.

[35] L. Chaal, C. Debiemme-Chouvy, C. Deslouis, G. Maurin, A. Pailleret, B. Saidani, Comparative AFM nanoscratching tests in air of bulk copper and electrogenerated cuprous oxide films, Surf. Sci. 605 (2011) 121–130.

[36] N. Cherchour, C. Deslouis, B. Messaoudi, A. Pailleret, PH sensing in aqueous solutions using a MnO2 thin film electrodeposited on a glassy carbon electrode, Electrochim. Acta. 56 (2011) 9746–9755. https://doi.org/10.1016/j.electacta.2011.08.011.

[37] H. Chen, Z. Wei, X. Zheng, S. Yang, A scalable electrodeposition route to the low-cost, versatile and controllable fabrication of perovskite solar cells, Nano Energy. 15 (2015) 216–226. https://doi.org/10.1016/j.nanoen.2015.04.025.

[38] X.P. Cui, K.J. Jiang, J.H. Huang, X.Q. Zhou, M.J. Su, S.G. Li, Q.Q. Zhang, L.M. Yang, Y.L. Song, Electrodeposition of PbO and its in situ conversion to CH3NH3PbI3 for mesoscopic perovskite solar cells, Chem. Commun. 51 (2015) 1457–1460. https://doi.org/10.1039/c4cc08269a.

[39] J.H. Huang, K.J. Jiang, X.P. Cui, Q.Q. Zhang, M. Gao, M.J. Su, L.M. Yang, Y. Song, Direct Conversion of CH 3 NH 3 PbI 3 from Electrodeposited PbO for Highly Efficient Planar Perovskite Solar Cells, Sci. Rep. 5 (2015) 1–8. https://doi.org/10.1038/srep15889.

[40] G.H.A. Therese, P. V. Kamath, Electrochemical synthesis of metal oxides and hydroxides, Chem. Mater. 12 (2000) 1195–1204. https://doi.org/10.1021/cm990447a.

[41] W.Q. Hong, Extraction of extinction coefficient of weak absorbing thin films from

special absorption, J. Phys. D. Appl. Phys. 22 (1989) 1384–1385. https://doi.org/10.1088/0022-3727/22/9/024.

[42] G. Popov, M. Mattinen, M.L. Kemell, M. Ritala, M. Leskela, Scalable route to the fabrication of CH3NH3PbI3 perovskite thin films by electrodeposition and vapor conversion, ACS Omega. 1 (2016) 1296–1306. https://doi.org/10.1021/acsomega.6b00351.

[43] I. Dhiaputra, B. Permana, Y. Maulana, Y.D. Inayatie, Y.R. Purba, A. Bahtiar, Composition and crystal structure of perovskite films attained from electrodes of used car battery, AIP Conf. Proc. 1712 (2016) 1–6. https://doi.org/10.1063/1.4941896.

[44] Q. Lin, A. Armin, R.C.R. Nagiri, P.L. Burn, P. Meredith, Electro-optics of perovskite solar cells, Nat. Photonics. 9 (2015) 106–112. https://doi.org/10.1038/nphoton.2014.284.

[45] Z. Su, F. Hou, F. Jin, L. Wang, Y. Li, J. Zhu, B. Chu, W. Li, Hole transporting material-free and annealing-free thermal evaporated planar perovskite solar cells with an ultra-thin CH3NH3PbI3-XClX layer, Org. Electron. 26 (2015) 104–108. https://doi.org/10.1016/j.orgel.2015.07.028.

[46] D. Song, P. Cui, T. Wang, D. Wei, M. Li, F. Cao, X. Yue, P. Fu, Y. Li, Y. He, B. Jiang, M. Trevor, Managing Carrier Lifetime and Doping Property of Lead Halide Perovskite by Postannealing Processes for Highly Efficient Perovskite Solar Cells, J. Phys. Chem. C. 119 (2015) 22812–22819. https://doi.org/10.1021/acs.jpcc.5b06859.

[47] J.M.C. Da Silva Filho, F.C. Marques, Growth of Perovskite Nanorods from PbS Quantum Dots, MRS Adv. 3 (2018) 1843–1848. https://doi.org/10.1557/adv.2018.188.

[48] A. Ummadisingu, L. Steier, J.Y. Seo, T. Matsui, A. Abate, W. Tress, M. Grätzel, The effect of illumination on the formation of metal halide perovskite films, Nature. 545 (2017) 208–212. https://doi.org/10.1038/nature22072.

[49] B.D. Viezbicke, S. Patel, B.E. Davis, D.P. Birnie, Evaluation of the Tauc method for optical absorption edge determination: ZnO thin films as a model system, Phys. Status Solidi Basic Res. 252 (2015) 1700–1710. https://doi.org/10.1002/pssb.201552007.

[50] O. Almora, C. Aranda, E. Mas-Marzá, G. Garcia-Belmonte, On Mott-Schottky analysis interpretation of capacitance measurements in organometal perovskite solar cells, Appl. Phys. Lett. 109 (2016). https://doi.org/10.1063/1.4966127.

[51] W.A. Laban, L. Etgar, Depleted hole conductor-free lead halide iodide heterojunction solar cells, Energy Environ. Sci. 6 (2013) 3249–3253. https://doi.org/10.1039/c3ee42282h.

[52] R. van de Krol, A. Goossens, J. Schoonman, Mott - Schottky Analysis of Nanometer - Scale Thin - Film Anatase TiO 2 Mott-Schottky Analysis of Nanometer-Scale, J. Electrochem. Soc. 144 (1997) 1723–1727.

[53] W. Liu, Y. Zhang, Electrical characterization of TiO2/CH3NH 3PbI3 heterojunction solar cells, J. Mater. Chem. A. 2 (2014) 10244–10249. https://doi.org/10.1039/c4ta01219d.

[54] F. Liu, Q. Dong, M.K. Wong, A.B. Djurišić, A. Ng, Z. Ren, Q. Shen, C. Surya, W.K. Chan, J. Wang, A.M.C. Ng, C. Liao, H. Li, K. Shih, C. Wei, H. Su, J. Dai, Is Excess PbI2 Beneficial for Perovskite Solar Cell Performance?, Adv. Energy Mater. 6 (2016) 1–9. https://doi.org/10.1002/aenm.201502206.

HIGHLIGHTS

- $CH_3NH_3PbI_3$ perovskite thin films were synthesized using electrodeposition and two chemical conversion steps
- They are p-type semiconductors with a bandgap energy close to 1.57 eV
- They all contain a PbI_2 fraction that depends on the two immersion durations
- When the PbI_2 % decreases, the carrier concentration increases over three decades
- Our synthesis method is promising for the fast and large scale production of tunable perovskites

Declaration of interests

☒ The authors declare that they have no known competing financial interests or personal relationships that could have appeared to influence the work reported in this paper.

☐ The authors declare the following financial interests/personal relationships which may be considered as potential competing interests: